# One-step *in situ* Controllable Synthesis
# of MnFe$_2$O$_4$/rGO Nanocomposite and Its Application
# to Electrochemical Sensing of Hydrogen Peroxide

Xueling Zhao,[1,2] Beilei Xie,[1] Zhanhong Li,[1,2] Cheng Chen,[1,2] and Zhigang Zhu[1,2*]

[1]School of Environmental and Materials Engineering, College of Engineering, Shanghai Polytechnic University
2360 Jinhai Road, Shanghai 201209, P. R. China
[2]Research Center of Resource Recycling Science and Engineering, Shanghai Polytechnic University
2360 Jinhai Road, Shanghai 201209, P. R. China

In this work, we prepared a reduced graphene oxide (rGO)-supported manganese ferrite (MnFe$_2$O$_4$) hybrid material by a simple one-pot solvothermal synthesis method, using graphite oxide (GO) and metal ions (Fe$^{3+}$, Mn$^{2+}$) as raw materials. The reduction of GO and the *in situ* formation of MnFe$_2$O$_4$ nanoparticles were simultaneously achieved during the synthesis. The properties of MnFe$_2$O$_4$/rGO were characterized by scanning electron microscopy, powder X-ray diffraction, Fourier-transform infrared spectroscopy, and energy-dispersive X-ray spectrometry. The electrochemical characterizations of the resulting sensor were carried out by cyclic voltammetry and chronoamperometry. The results of electrochemical experiments show that the composite has improved hydrogen peroxide (H$_2$O$_2$) reduction performance. The linear range of the as-prepared sensor for H$_2$O$_2$ detection is 0.025 to 1.5 mM, with a detection limit of 0.796 μM (S/N = 3) and a response time of less than 4 s. In this paper, an effective, economical, and green experimental method for the synthesis of metal-oxide/graphene nanocomposites is proposed.

## 1. Introduction

Hydrogen peroxide (H$_2$O$_2$) plays an important role in life activities and pharmaceutical, environmental, and industrial processes.[1–3] It is also an important by-product of many oxidation reactions (active oxygen) and is a major pollutant in the environment.[4–6] In living organisms, living cells secrete H$_2$O$_2$ in the mitochondria to regulate the normal function of the cells.[7] H$_2$O$_2$ is also closely related to aging and nervous system diseases. Therefore, the construction of a controllable, low-cost, and rapid H$_2$O$_2$-response recognition system has attracted widespread attention.[8]

Since Gao *et al.*[9] reported, for the first time, that ferromagnetic nanoparticles have mimetic enzymes similar to common peroxidases, many research groups have begun to

---

study the catalysis of magnetic materials on $H_2O_2$ by spectroscopy[10] and electrochemical methods.[11] $M$Fe$_2$O$_4$ ($M$ = Co, Mn, Zn, Ni, Cu, etc.), which has a cubic spinel structure, is an important ferromagnetic nanomaterial.[12] It has shown a great application value in the fields of information storage, pollutant removal, medical diagnosis, and drug delivery.[13] However, unmodified spinel-type ferromagnetic particles are easily agglomerated and extremely unstable, so their applications are also facing enormous challenges. In addition, sensors based on $M$Fe$_2$O$_4$ usually have problems such as low sensitivity and narrow linear range.[14,15] Therefore, it is necessary to modify the surfaces of magnetic nanoparticles by an appropriate method to overcome these limitations.[16,17]

A two-dimensional layered nanomaterial, graphene, has received extensive attention owing to its unique electrical, thermal, mechanical, and chemical properties, and has good application prospects in environmental detection and repair, energy conversion, energy storage, and biosensing.[18–20] Therefore, the combination of graphene and $M$Fe$_2$O$_4$ magnetic nanoparticles can not only enhance the electrocatalytic activity and electron transfer ability of the material, but also prevent the agglomeration of magnetic nanoparticles, which makes it an ideal sensing platform for electrochemical sensors/biosensors.[21–23] Unfortunately, the controlled synthesis of $M$Fe$_2$O$_4$ nanoparticles on reduced graphene oxide (rGO) nanosheets remains a challenge.

Herein, we prepared MnFe$_2$O$_4$/rGO by a one-pot solvothermal process using GO and metal chlorides as raw materials. The morphology and structure of the nanocomposites were investigated. In addition, the catalytic properties, including the reduction of $H_2O_2$, were systematically investigated.

## 2.   Experimental Methods

### 2.1   Materials

Graphite powder, iron (III) chloride hexahydrate (FeCl$_3$·6H$_2$O), manganese chloride tetrahydrate (MnCl$_2$·4H$_2$O), polyethylene glycol (PEG), ethylene glycol (EG), and $H_2O_2$ were purchased from Sinopharm Chemical Reagent Co., Ltd. Dopamine (DA), ascorbic acid (AA), uric acid (UA), and glucose (Glu) were obtained from Sigma-Aldrich. All other chemicals and reagents were of the analytical grade and employed without any additional purification.

### 2.2   Preparation of MnFe$_2$O$_4$/rGO

The synthesis method for MnFe$_2$O$_4$/rGO nanocomposites is as follows.[24] Certain amounts of NaAc and PEG are added to the EG dispersion of 2 mg/mL GO, 0.04 M FeCl$_3$·6H$_2$O, and 0.02 M MnCl$_2$·4H$_2$O. After stirring for a certain period of time, the mixture is transferred to a hydrothermal reaction kettle and heated at 200 °C for 10 h. The final product is centrifuged and washed with ethanol several times and dried in a vacuum oven at 60 °C. Additionally, MnFe$_2$O$_4$ bare spheres and pure rGO are prepared under the same experimental conditions.

## 2.3 Preparation of the modified electrodes

Our laboratory-made screen-printed carbon electrodes (SPCEs) were used as substrates for immobilized catalysts. The printing and processing methods for SPCEs were described in our previous work.[25] The modified electrodes were dried and stored in a desiccator for later use. The $MnFe_2O_4$, rGO, and $MnFe_2O_4$/rGO nanostructure-modified electrodes are specified as $MnFe_2O_4$/SPCE, rGO/SPCE, and $MnFe_2O_4$/rGO/SPCE, respectively.

## 2.4 Material characterizations

Morphological and structural properties of the synthesized nanocomposites were characterized by powder X-ray diffraction (XRD, D8-Advance, Bruker, Germany), scanning electron microscopy (SEM, SU8220, Hitachi Co., Ltd, Japan), Fourier-transform infrared spectroscopy (FTIR, Nicolet 6700, USA), and energy-dispersive X-ray spectrometry (EDS) with SEM.

## 2.5 Electrochemical measurements

Cyclic voltammetry (CV), amperometry measurements, and electrochemical impedance spectroscopy (EIS) were carried out on a CHI-760E electrochemical workstation (CH Instruments, Shanghai, China). The three-electrode system consisted of a screen-printed electrode, a platinum wire, and an SCE as the working, auxiliary, and reference electrodes, respectively. All electrochemical tests were performed in 0.1 M PBS (pH 7.4). Additionally, prior to testing, all solutions were bubbled with high-purity nitrogen for 15 min to completely remove oxygen.

## 3. Results and Discussion

In this work, a simple *in situ* synthesis method was adopted to prepare $MnFe_2O_4$/rGO. The whole process is as follows: GO is first exfoliated by an ultrasonic method, and then the $MnFe_2O_4$ microspheres simultaneously grow on the rGO nanosheets during the solvothermal process. The mechanism associated with structural transformation is that, during the dispersion of the raw materials, $Fe^{3+}$ and $Mn^{2+}$ cations are adsorbed on the negatively charged GO surface as nucleation sites by electrostatic interaction. Subsequently, in the hydrothermal process, EG and PEG are used as both solvents and reducing agents. NaAc can change the alkalinity of the solution, which causes $Fe^{3+}$ and $Mn^{2+}$ to grow into $MnFe_2O_4$ nanocrystallites under alkaline conditions and further aggregate into microspheres.

## 3.1 Characterization of samples

The morphology of $MnFe_2O_4$/rGO nanocomposites was characterized by SEM. It can be seen from Fig. 1 that $MnFe_2O_4$ microspheres with a uniform size and an average diameter of
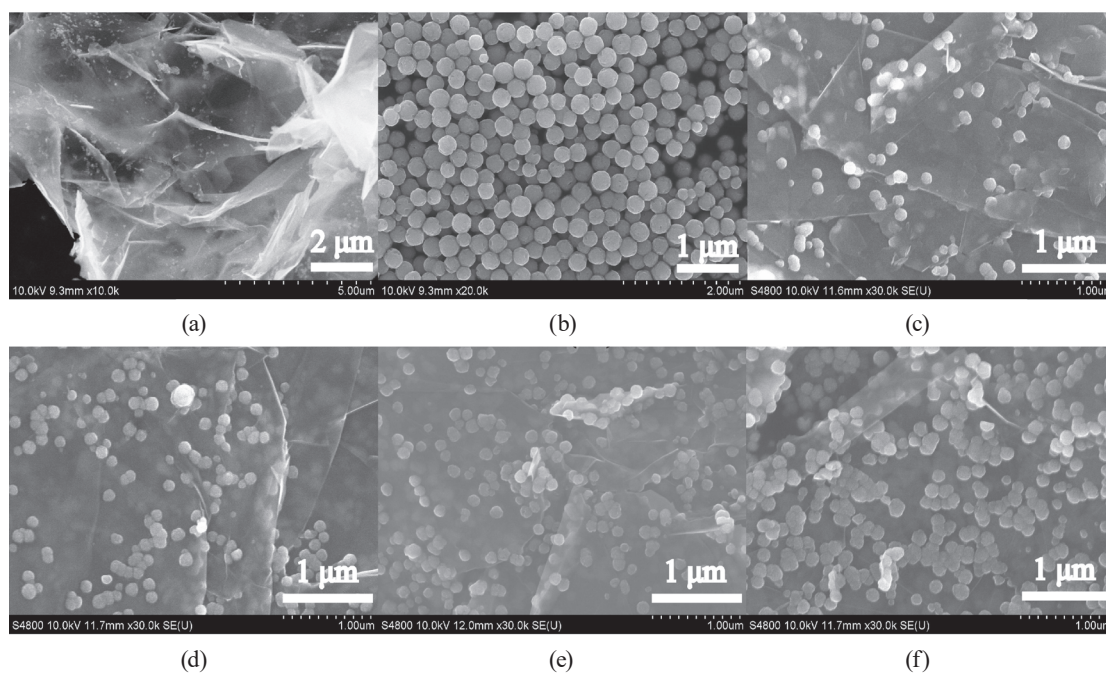
Fig. 1. SEM images of (a) GO, (b) $MnFe_2O_4$, (c) $MnFe_2O_4$/rGO-1/2, (d) $MnFe_2O_4$/rGO, (e) $MnFe_2O_4$/rGO-2, and (f) $MnFe_2O_4$/rGO-3.

about 120 nm are coated on the surfaces of rGO nanosheets [Fig. 1(d)]. In fact, the concentration of metal ions determines the size and distribution density of $MnFe_2O_4$ microspheres on rGO nanosheets. For comparison, we also synthesized the $MnFe_2O_4$/rGO nanocomposites with half [$MnFe_2O_4$/rGO-1/2, Fig. 1(c)], twice [$MnFe_2O_4$/rGO-2, Fig. 1(e)], and triple [$MnFe_2O_4$/rGO-3, Fig. 1(f)] the metal ion concentration previously used while maintaining the other conditions. As shown in Figs. 1(c)–1(f), the density of $MnFe_2O_4$ microspheres on rGO nanosheets increases significantly with the metal ion concentration. The size of $MnFe_2O_4$ microspheres in $MnFe_2O_4$/ rGO-1/2 and $MnFe_2O_4$/rGO samples is about 120 nm. However, in the $MnFe_2O_4$/rGO-2 and $MnFe_2O_4$/rGO-3 nanocomposites, the size of $MnFe_2O_4$ microspheres is about 150 nm, which is significantly larger than the sample size obtained with lower metal ion concentrations. One possible reason is that the increase in metal ion concentration will increase the number of $MnFe_2O_4$ nanocrystallites, thereby increasing the density and size of $MnFe_2O_4$ microspheres on rGO nanosheets. The SEM image of the bare $MnFe_2O_4$ microspheres prepared without GO is shown in Fig. 1(b). These microspheres have good monodispersity and their diameter is larger than that of the $MnFe_2O_4$ microspheres in the $MnFe_2O_4$/rGO nanocomposite.

The XRD pattern of the synthetic $MnFe_2O_4$/rGO nanocomposite is shown in Fig. 2(a). The disappearance of the peak at $2\theta = 10.3°$ indicates the removal of the oxygen-containing group, and GO is reduced to rGO. This conclusion can also be confirmed by FTIR spectroscopy. The diffraction peaks at 18.3, 30.1, 35.4, 43.1, 53.7, 56.9, and 62.5° correspond to the (111), (220), (311), (400), (422), (511), and (440) crystal planes of cubic spinel $MnFe_2O_4$ (JCPDS 74-2403). In addition, we further confirmed the composition of the nanocomposites by EDS. The results
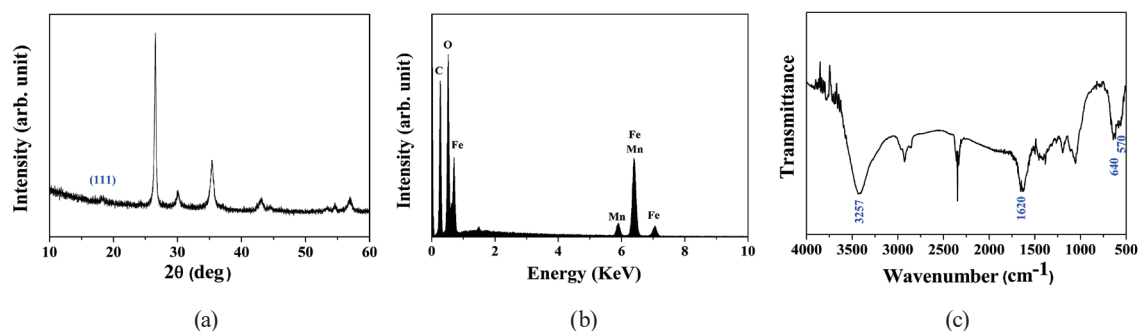
Fig. 2.    (a) XRD pattern and (b) EDS and (c) FTIR spectra of $MnFe_2O_4$/rGO nanocomposite.

show that the nanocomposites contain the elements Mn, Fe, C, and O [Fig. 2(b)], in which C is mainly derived from rGO nanosheets and O is derived from oxygen-containing functional groups of $MnFe_2O_4$ and rGO.

The chemical structure of $MnFe_2O_4$/rGO nanocomposites was investigated by FTIR spectroscopy [Fig. 2(c)]. Among them, the absorption band at 3457 $cm^{-1}$ is derived from the tensile and deformation vibrations of O–H. The peaks at 1739 and 1620 $cm^{-1}$ are derived from ketone (C=O) and carboxyl (COOH) functional groups. However, in the FTIR spectrum of the $MnFe_2O_4$/rGO nanocomposite, the absorption associated with the oxygen-containing group disappears or decreases greatly, indicating the reduction of GO. In addition, lattice absorption peaks ($M$ = Fe and Mn) from $M$–O are observed at 640 and 570 $cm^{-1}$, confirming the presence of $MnFe_2O_4$ in the sample.

## 3.2    Electrochemical sensing of $H_2O_2$

The electrocatalytic activity of the developed $MnFe_2O_4$/rGO nanocomposites for $H_2O_2$ detection was evaluated by a CV technique within a potential range from −0.9 to +1.0 V in 0.1 M PBS with a scan rate of 50 mV/s. Figure 3(a) shows the cyclic voltammetric behavior of $MnFe_2O_4$/rGO/SPCE in the presence or absence of $H_2O_2$. As shown, a pair of redox peaks are observed on $MnFe_2O_4$/rGO/SPCE. After adding $H_2O_2$, the reduction peak current of $MnFe_2O_4$/rGO/SPCE increases at −0.5 V, indicating that the prepared electrode has a distinct ability to accomplish electrochemical reduction to $H_2O_2$.

In order to compare the electrochemical response behaviors of electrodes modified with different materials with $H_2O_2$, CV curves of rGO/SPCE, $MnFe_2O_4$/SPCE, and $MnFe_2O_4$/rGO/ SPCE were recorded in 0.1 M PBS against 0.2 mM $H_2O_2$. As shown in Fig. 3(b), $MnFe_2O_4$/ rGO/SPCE shows a larger reduction peak than rGO/SPCE and $MnFe_2O_4$/SPCE. The excellent electrocatalytic activity of $MnFe_2O_4$/rGO/SPCE can be derived from the good synergistic effect between $MnFe_2O_4$ microspheres and rGO nanosheets for the following reasons. On the one hand, $MnFe_2O_4$ microspheres are attached to or distributed over the rGO nanosheets, which can inhibit the agglomeration of the magnetic nanoparticles and the curling of the sheet structure, thereby increasing the effective area of the composite. On the other hand, the rGO nanosheets are formed as the core of $MnFe_2O_4$ magnetic microspheres. The nuclear matrix can induce the
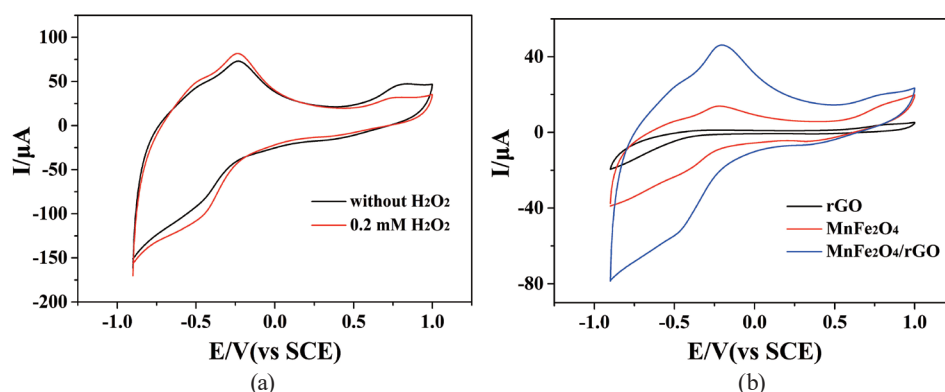
Fig. 3. (Color online) (a) CV curves of MnFe$_2$O$_4$/rGO/SPCE in absence and presence of H$_2$O$_2$ in 0.1 M PBS (pH 7.4) with a scan rate of 50 mV/s. (b) CV curves of rGO/SPCE, MnFe$_2$O$_4$/SPCE, and MnFe$_2$O$_4$/rGO/SPCE in 0.1 M PBS with a scan rate of 50 mV/s.
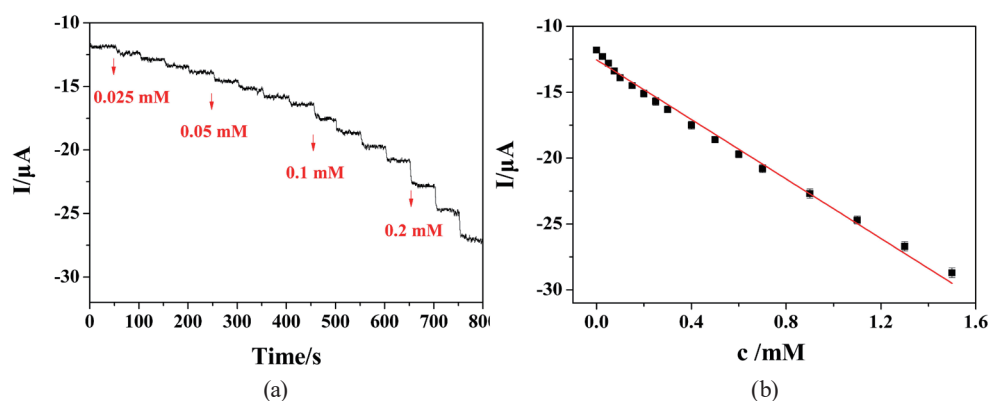


Fig. 4. (Color online) (a) Amperometric response of MnFe$_2$O$_4$/rGO/SPCE with consecutive additions of different concentrations of H$_2$O$_2$ into 0.1 M PBS (pH 7.4) at an applied potential of −0.5 V vs SCE. (b) Relevant calibration curves of H$_2$O$_2$ concentration vs peak current.

nucleation and growth distribution of the nanocrystals, form fine nanostructures, and uniformly disperse and control the morphology on the surface of the lamellar structure through chemical functions. Thus, a perfect overall structure can be formed between the MnFe$_2$O$_4$ magnetic microspheres and the rGO nanosheets. This structure is a conductive network that can shorten the path of electron and ion transport.

Figure 4 gives the amperometric response of MnFe$_2$O$_4$/rGO/SPCE to different H$_2$O$_2$ concentrations at −0.5 V vs SCE in 0.1 M PBS (pH 7.4). It can be seen from the figure that with the consecutive injection of H$_2$O$_2$, the current response increases stepwise while the response time is about 4 s. The results indicate a rapid electron transfer between the electrode and H$_2$O$_2$. In the concentration range of 0.025 to 1.5 mM, the concentration of H$_2$O$_2$ showed a good linear relationship with the ampere response with a sensitivity of 0.113 mA/mM. In addition, the limit of detection of MnFe$_2$O$_4$/rGO/SPCE to H$_2$O$_2$ can be reduced to 0.796 μM (S/N = 3). From Table 1, it is clear that the electrochemical sensing performance characteristics of as-fabricated MnFe$_2$O$_4$/rGO/SPCE are analogous and even superior to those in the recent reports.[26–30]

Table 1
Comparison of the analytical performance characteristics of various electrodes for $H_2O_2$ sensing.

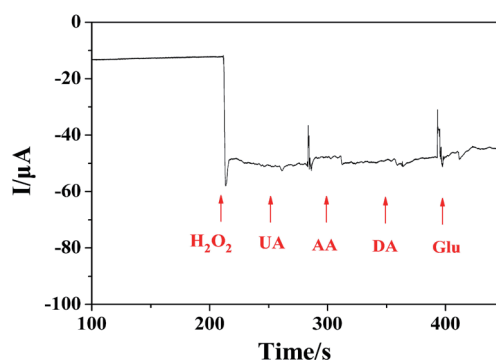| Electrode | Sensitivity ($\mu$A/mM) | LOD ($\mu$M) | Linear range ($\mu$M) | Ref. |
|---|---|---|---|---|
| $Fe_3O_4$/RGO/Hb | 0.0468 | 2 | 4–1000 | (26) |
| $Ce_{1-x}Tb_xO_y$/GCE | 1.683 | 7.7 | 0.1–4200 | (27) |
| (G-PAM)/GCE | 3.5 | 35 | 250–2250 | (28) |
| Cyt.c/Ni foam | 1.92 | 0.2 | 20–250 | (29) |
| Cu/ITO/FTO | 73.7 | 60 | 100–1000 | (30) |
| $MnFe_2O_4$/rGO/SPCE | 113 | 0.796 | 25–1500 | This work |



Fig. 5.    (Color online) Amperometric response upon successive addition of UA, AA, DA, Glu, and $H_2O_2$ at −0.5 V in 20 mL PBS.

Selectivity is an important indicator for evaluating the performance of nonenzymatic electrochemical sensors. In actual samples, UA, AA, DA, and Glu usually coexist with $H_2O_2$ and may cause interference during the detection of $H_2O_2$. Figure 5 shows the amperometric response curves after 0.1 mM $H_2O_2$ and 0.5 mM AA, UA, DA, and Glu were continuously added to 0.1 M PBS (pH 7.4). As shown by the figure, the above interfering substances have no significant effect on the detection of $H_2O_2$. This result reveals that the $MnFe_2O_4$/rGO nanocomposite-modified electrode exhibits excellent selectivity for $H_2O_2$ and can be used for its detection in actual samples.

## 4.    Conclusions

We successfully prepared $MnFe_2O_4$/rGO nanocomposites by a simple one-step solvothermal method. The reduction of GO and the growth of $MnFe_2O_4$ were simultaneously achieved during the synthesis. In addition, by changing the metal ion concentration in the raw material, the size of the $MnFe_2O_4$ microspheres and the dispersion density on the rGO nanosheets are well controlled. Because of the excellent biocompatibility and good synergy between $MnFe_2O_4$ and rGO, the prepared nanocomposites of $MnFe_2O_4$/rGO have high selectivity and sensitivity (0.113 mA/mM), a large linear range (0.025 to 1.5 mM), and a lower detection limit (0.796 $\mu$M). This sensor can be used as an effective tool for the qualitative and quantitative monitoring of dynamic changes in $H_2O_2$ concentration in different systems.

## Acknowledgments

## References

1 Q. Chen, L. Z. Feng, J. J. Liu, W. W. Zhu, Z. L. Dong, Y. F. Wu, and Z. Liu: Adv. Mater. **28** (2016) 7129. https://doi.org/10.1002/adma.201601902

2 F. Y. Xie, X. Q. Cao, F. L. Qu, A. M. Asiri, and X. P. Sun: Sensor Actuat., B **255** (2018) 1254. https://doi.org/10.1016/j.snb.2017.08.098

3 R. M. Song, Z. H. Li, P. J. Wei, X. L. Zhao, C. Chen, and Z.G. Zhu: Appl. Sci. **8** (2018) 848. https://doi.org/10.3390/app8060848

4 C. Zhang, W. H. Chen, L. H. Liu, W. X. Qiu, W. Y. Yu, and X. Z. Zhang: Adv. Funct. Mater. **10** (2017) 1700626. https://doi.org/10.1002/adfm.201700626

5 W. P. Li, C. H. Su, Y. C. Chang, Y. J. Lin, and C. S. Yeh: ACS Nano **10** (2016) 2017. https://doi.org/10.1021/acsnano.5b06175

6 S. Kogularasu, M. Govindasamy, S. M. Chen, M. Akilarasan, and V. Mani: Sensor Actuat., B **253** (2017) 773. https://doi.org/10.1016/j.snb.2017.06.172

7 Y. Sun, K. He, Z. Zhang, A. Zhou, and H. Duan: Biosens. Bioelectron. **68** (2015) 358. https://doi.org/10.1016/j.bios.2015.01.017

8 R. Umamaheswari, M. Akilarasan, S. Chen, Y. Cheng, V. Mani, S. Kogularasu, F. AlHemaid, A. M. Ajmal, and X. Liu: J. Colloid. Interf. Sci. **505** (2017) 1193. https://doi.org/10.1016/j.jcis.2017.07.006

9 L. Z. Gao, J. Zhuang, L. Nie, J. B. Zhang, Y. Zhang, N. Gu, T. H. Wang, J. Feng, D. L. Yang, S. Perrett, and X. Y. Yan: Nat. Nanotechnol. **2** (2007) 577. https://doi.org/10.1038/nnano.2007.260

10 K. Yang, H. Zhong, Z. P. Cheng, X. R. Li, A. R. Zhang, T. L. Li, Y. J. Zhang, G. Q. Liu, and H. Y. Qian: J. Electroanal. Chem. **814** (2018). 1. https://doi.org/10.1016/j.jelechem.2018.02.040

11 X. L. Zhao, Z. H. Li, C. Chen, Y. H. Wu, Z. G. Zhu, H. L. Zhao, and M. B. Lan: Electroanalysis **29** (2017) 1518. https://doi.org/10.1002/elan.201600793

12 C. Pereira, R. S. Costa, L. Lopes, B. B. Baeza, I. R. Ramos, A. G. Ruiz, P. B. Tavares, C. Freire, and A. M. Pereira: Nanoscale **10** (2018) 12820. https://doi.org/10.1039/C8NR03533D

13 R. A. Henning, P. Uredat, C. Simon, A. Bloesser, P. Cop, M. T. Elm, and R. Marschall: J. Phys. Chem., C. **123** (2019) 18240. https://doi.org/10.1021/acs.jpcc.9b04635

14 M. Lin and H. Leu: Electroanalysis **17** (2005) 2068. https://doi.org/10.1002/elan.200503335

15 G. J. Rani, K. J. Babu, G. G. Kumar, and M. A. J. Ragan: J. Alloy. Compd. **688** (2016) 500. https://doi.org/10.1016/j.jallcom.2016.07.101

16 X. Zhu, H. L. Zhao, X. H. Niu, T. T. Liu, L. B. Shi, and M. B. Lan: Microchim. Acta. **183** (2016) 2431. https://doi.org/10.1007/s00604-016-1887-3

17 C. Pereira, R. S. Costa, L. Lopes, B. B. Baeza, I. R. Ramos, A. G. Ruiz, P. B. Tavares, C. Freire, and A. M. Pereira: Nanoscale **11** (2019) 3397. https://doi.org/10.1039/C9NR90031D

18 D. Li and K. B. Kaner: Science **320** (2008) 1170. https://doi.org/10.1126/science.1158180

19 Y. L. Shao, M. F. Ei-Kady, L. J. Wang, Q. H. Zhang, Y. G. Li, H. Z. Wang, M. F. Mousavi, and R. B. Kaner: Chem. Soc. Rev. **44** (2015) 3639. https://doi.org/10.1039/C4CS00316K

20 Z. G. Zhu, L. Garcia-Gancedo, A. J. Flewitt, H. Q. Xie, F. Moussy, and W. I. Milne: Sensors 12 □2012□5996. https://doi.org/10.3390/s120505996

21 C. L. Justino, A. Gomes, A. C. Freitas, A. C. Duarte, and T. A. Rocha-Santos: Trac-Trend. Anal. Chem. **91** (2017) 53. https://doi.org/10.1016/j.trac.2017.04.003

22 L. Zhou, H. J. Mao, C. Y. Wu, L. Tang, Z. H. Wu, H. Sun, H. L. Zhang, H. B. Zhou, C. P. Jia, Q. H. Jin, X. F. Chen, and J. L. Zhao: Biosens. Bioelectron. **15** (2017) 701. https://doi.org/10.1016/j.bios.2016.09.025

23 P. J. Wei, Z. G. Zhu, R. M. Song, Z. H. Li and C. Chen: Electrochimica Acta **317** (2019) 93. https://doi.org/10.1016/j.electacta.2019.05.136

24   S. Bai, X. P. Shen, X. Zhong, Y. Liu, G. X. Zhu, X. Xu, and K. M. Chen: Carbon **50** (2012) 2337. https://doi. org/10.1016/j.carbon.2012.01.057

25   X. H. Niu, C. Chen , H. L. Zhao, J. Tang, Y. X. Li and M. B. Lan: Electrochem. Commun. **22** (2012) 170. https://doi.org/10.1016/j.elecom.2012.06.020

26   S. M. Zhu, J. J. Guo, J. P. Dong, Z. W. Cui, T. Lu, C. L. Zhu, D. Zhang, and J. Ma: Ultrason. Sonochem. **3** (2013) 872. https://doi.org/10.1016/j.ultsonch.2012.12.001

27   L. Zhao, K. Sun, N. Youliwasi, H. L. Guo, G. Yang, F. Jiao, B. Dong, Y. M. Chai, S. Mintova, and C. G. Liu: Appl. Surf. Sci. **15** (2019) 91. https://doi.org/10.1016/j.apsusc.2018.10.278

28   A. J. Xie, Q. X. Liu, H. L. Ge, and Y. Kong. Mater. Technol. Advanced Perform. Mater. **30** (2015) 50. https:// doi.org/10.1179/1753555714Y.0000000203

29   N. Akhtar, S. A. EI-Safty, M. Khairy, and W. A. EI-Said: Sens. Actuators., B **207** (2015) 158. https://doi. org/10.1016/j.snb.2014.10.038

30   M. Rehosek, D. Mitoraj, M. Bledowski, and R. Beranek: Electroanalysis **10** (2016) 2327. https://doi. org/10.1002/elan.201600227